

Mapping the Ultrafast Mechanistic Pathways of Co Photocatalysts in Pure Water through Time-Resolved X-ray Spectroscopy

Lucia Velasco,^[a] Cunming Liu,^[b] Xiaoyi Zhang,^[b] Sergi Grau,^[c] Marcos Gil-Sepulcre,^[c] Carolina Gimbert-Suriñach,^[c, e] Antonio Picón,^[d] Antoni Llobet,^[c, e] Serena DeBeer,^[f] and Dooshaye Moonshiram^{*[a]}

Nanosecond time-resolved X-ray (tr-XAS) and optical transient absorption spectroscopy (OTA) are applied to study 3 multi-molecular photocatalytic systems with [Ru(bpy)₃]²⁺ photoabsorber, ascorbic acid electron donor and Co catalysts with methylene (1), hydroxomethylene (2) and methyl (3) amine substituents in pure water. OTA and tr-XAS of 1 and 2 show that the favored catalytic pathway involves reductive quenching of the excited photosensitizer and electron transfer to the catalyst to form a Co^{II} square pyramidal intermediate with a

bonded aqua molecule followed by a Co^I square planar derivative that decays within $\approx 8 \mu\text{s}$. By contrast, a Co^I square pyramidal intermediate with a longer decay lifetime of $\approx 35 \mu\text{s}$ is formed from an analogous Co^{II} geometry for 3 in H₂O. These results highlight the protonation of Co^I to form the elusive hydride species to be the rate limiting step and show that the catalytic rate can be enhanced through hydrogen containing pendant amines that act as H–H bond formation proton relays.

Introduction

The search for sustainable ways to store and distribute energy is one of the most urgent scientific challenges in view of the rapid depletion of fossil fuels, environmental pollution and

resulting climate emergency.^[1] A solution to the undergoing energy crisis can only be obtained through implementation of renewable sources and new low-polluting fuels.^[2] Solar-driven water splitting provides an efficient means of meeting our energy demands and storing energy in the form of a clean fuel (H₂) and oxidant (O₂).^[3] Hydrogen as an energy carrier further provides an attractive alternative to fossil fuels with its combustion producing only heat and water.^[2,4]

The prospect of developing a hydrogen economy and using hydrogen as a carbon-free fuel has motivated the discovery of effective and robust catalysts that can lower the energy barriers to hydrogen production. Molecular earth-abundant hydrogen evolution catalysts (HECs) such as cobalt,^[5] nickel,^[6] molybdenum^[7] and iron,^[8] have particularly become a prime focus of research due to their low costs and potential viabilities for a future hydrogen fuel technology. Approaches similar to natural photosynthetic modules have further been developed to efficiently couple photosensitizers which involve transient one-electron excited states to multi-electron, proton-coupled earth-abundant HECs.^[9] However, despite significant efforts, much of the emphasis has been based on studies conducted in non-aqueous media^[3,10] in which protons are supplied in the form of weak or strong acids rather than pure water. Some elegant approaches in generating water-soluble HECs lie in incorporating nitrogen donor ligands, modifying the carbon backbone of the ancillary ligand with polar hydroxy functionalities or introducing neutral axial ligands that aid towards design of cationic complexes.^[11] For instance, Sun et al.^[12] reported cationic Co complexes with polypyridyl ligands that were soluble in pure aqueous medium and could reach 100% faradaic efficiency and turnover numbers (TONs) of 5.5×10^4 . Similarly, Co electrocatalytic^[11] and photocatalytic tetraazamacrocycles^[13] HECs illustrated faradaic efficiencies

[a] L. Velasco, Dr. D. Moonshiram

Instituto de Ciencia de Materiales de Madrid
Consejo Superior de Investigaciones Científicas
Sor Juana Inés de la Cruz, 3, 28049, Madrid (Spain)
E-mail: dooshaye.moonshiram@csic.es
Homepage: <https://moonshiram.wordpress.com>

[b] Dr. C. Liu, Dr. X. Zhang

X-ray Science Division
Argonne National Laboratory
9700 S. Cass Avenue, Lemont IL, 60439 (U.S.A)

[c] Dr. S. Grau, Dr. M. Gil-Sepulcre, Dr. C. Gimbert-Suriñach, Prof. Dr. A. Llobet

Institute of Chemical Research of Catalonia (ICIQ)
Avinguda Països Catalans 16, 43007 Tarragona (Spain)

[d] Prof. Dr. A. Picón

Departamento de Química
Universidad Autónoma de Madrid
28049, Madrid (Spain)

[e] Dr. C. Gimbert-Suriñach, Prof. Dr. A. Llobet

Departament de Química
Universitat Autònoma de Barcelona
Cerdanyola del Vallès, 08193 Barcelona (Spain)

[f] Prof. Dr. S. DeBeer

Max Planck Institute for Chemical Energy Conversion
Stiftstr. 34–36, 45470 Mülheim an der Ruhr (Germany)

Supporting information for this article is available on the WWW under <https://doi.org/10.1002/cssc.202300719>

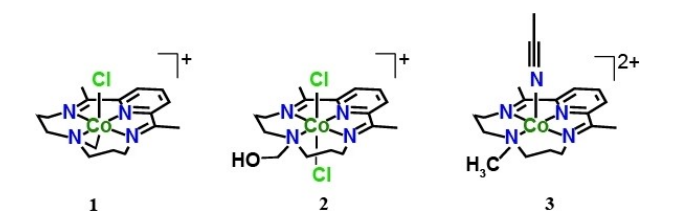
© 2023 The Authors. ChemSusChem published by Wiley-VCH GmbH. This is an open access article under the terms of the Creative Commons Attribution Non-Commercial NoDerivs License, which permits use and distribution in any medium, provided the original work is properly cited, the use is non-commercial and no modifications or adaptations are made.

close to 80% and TONs of 1000 at pH 4 in pure water. Within this group, one of the most used catalyst precursors is the $[\text{LCo}^{\text{III}}\text{Cl}_2]^+$ ($\text{L} = 2,12\text{-dimethyl-3,7,11,17-tetra-azabicyclo(11.3.1)-heptadeca-1(17),2,11,13,15-pentaene}$),^[13–14] which shows hour-long stabilities in pure water and can further encompass methylene, hydroxymethylene or methyl amine groups^[15] that are involved in the H_2 bond formation step (Scheme 1). The photocatalytic activities of these complexes^[15] were previously reported with the $[\text{Ru}(\text{bpy})_3]^{2+}$ ($\text{bpy} = 2,2'\text{-bipyridine}$) (Ru) photosensitizer, and their proposed hydrogen evolution pathways described through Density Functional Theoretical (DFT) calculations. However, key insights into the photo-induced electron transfer dynamics, photogenerated intermediates and influence of the various substituents on the amine groups of the Co-based catalysts (Scheme 1) that are responsible for their activities and essential for the fine-tuning of their electronic properties were not experimentally investigated, yet of crucial importance. Towards this aim, time-resolved X-ray absorption

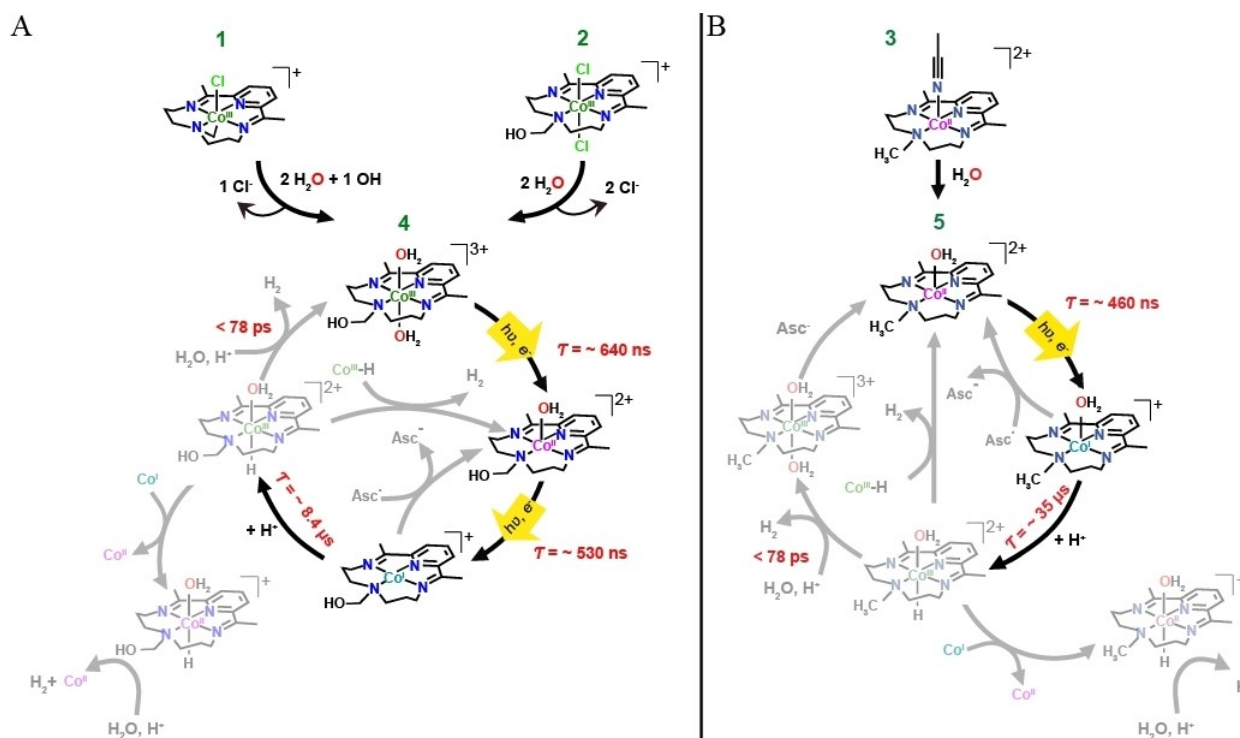
spectroscopy in the pico to microsecond time scale together with time-dependent DFT (TD-DFT) calculations are employed as powerful tools to map the kinetics, electronic and structural conformations of these 3 Co-based catalysts upon photo-excitation with Ru in pure water (Scheme 2).

The necessity to observe the dynamics of electron transfer processes in real time and retrieve the electronic and structural information of the involved transient states is critical for advancing our knowledge of the underlying mechanism. Commonly employed optical transient absorption spectroscopy (OTA) lacks element-specificity^[16] and cannot often identify the catalytic transient structures associated with the reaction dynamics due to the overwhelming fluorescence of the light-harvester, which masks the catalyst's absorption features. By contrast, pico-microsecond tr-XAS provides a powerful means of capturing transient intermediate snapshots all the way towards the hydrogen evolution reaction.^[14a,17] In this scenario, a laser pulse (pump) initiates a chemical reaction and an X-ray pulse (probe) at varying delays is used to interrogate its evolving electronic and structural response. This technique has considerably enhanced our fundamental understanding of photochemistry, solar energy conversion, interfacial electron transfer and biological enzymatic systems.^[14a,17a,18]

The catalysts are studied in binary mixtures with the Ru light-harvester as well as ternary mixtures with the addition of ascorbic acid as an electron donor. As shown in Scheme 2, catalyst 1 must be dissolved in water for at least 24 hours to be active. Upon dissolution in water, it adopts the same structural conformation as catalyst 2, that is a distorted octahedral



Scheme 1. Structures of the investigated Co-based catalyst precursors 1, 2 and 3 encompassing methylene, hydroxymethylene and methyl groups respectively.



Scheme 2. Mechanistic pathways for the Hydrogen evolution reaction catalyzed by the Co-based catalyst precursors 1 and 2 (A), 3 (B), and determined through corroborated tr-XAS spectroscopy and TD-DFT calculations. Catalytic intermediates shown in opaque lines were thoroughly investigated in this study. Determinations of the time constants shown in the scheme refer to those deduced from the tr-XAS experimental conditions in Figures 4D and Figures 5B–D.

geometry with two aqua ligands in the axial positions. We first start with a comparison of the steady-state structural conformations of the catalytic complexes in solid vs solution. Time-resolved XAS spectroscopy is subsequently applied to resolve the kinetics, electronic and structural conformations of the reactive Co^{II} , Co^{I} and protonation events as illustrated in Scheme 2.

Comparative kinetics analysis of the Co^{I} derivatives in **1**, **2** and **3** show that the pendant proton relay with the hydroxomethylene group plays a key role in facilitating the H–H bond formation. The experimental findings are thoroughly corroborated with time-dependent DFT (TD-DFT) to substantiate the photophysical processes occurring upon conversion of the Co^{III} catalysts into their reactive states.

The results reported here provide valuable insights on the reaction pathways and importance of the amine substituent groups on a family of highly versatile HECs and constitute an important step for the future development of earth-abundant water-soluble catalysts for photocatalytic applications.

Results and Discussion

Solid-state electronic and structural characterizations of the Co-based catalyst precursors

Steady-state X-ray absorption near edge structure (XANES) and extended X-ray absorption fine structure analysis (EXAFS) were first carried out on complexes **1**–**3** in solid state to gain comparative insights into their coordination behaviors and ground state structures prior to dissolution in solution (Figure 1).

The Co^{III} based compounds **1** and **2** display a main peak along the rising edge from 7710 to 7730 eV assigned as a $1s \rightarrow 4p$ transition with shakedown contributions (Figure 1A).^[19] These shakedown effects involve ligand to metal charge transfer states during the relaxation of the Co local electrons in the excited state and are sensitive to the metal-ligand bond covalency and influence of the donor character of the ligand.^[20,21] Catalyst **2** with two versus one chlorido ligands expectedly displays a more intense a ($1s \rightarrow 4p$ + shakedown) transition at 7722 eV in comparison to catalyst **1** at 7721 eV. By contrast, the Co^{II} catalyst **3** displays a weaker shoulder at 7715 eV assigned as a $1s \rightarrow 4p_z$ transition^[22] which reflects the nature of the $4p_z$ orbital in its penta-coordinated environment. It is important to remark that **3** does not show a strong negative energy shift compared to **1** and **2** due to its absence of chlorido ligands accounting for the $1s \rightarrow 4p$ shakedown transitions.

Interestingly, strong changes are additionally observed in the pre-edge region of the absorption spectra at lower photon energies around 7710 eV (Figure 1A inset). Presence of pre-edge features correspond to $1s$ to $3d$ quadrupole transitions and dipole excitations of the core electrons into the valence $3d$ states hybridized with ligand p orbitals.^[23,24] Although both Co^{III} catalysts **1** and **2** bear an octahedral geometry with a d^6 configuration, **1** displays a more intense pre-edge feature at

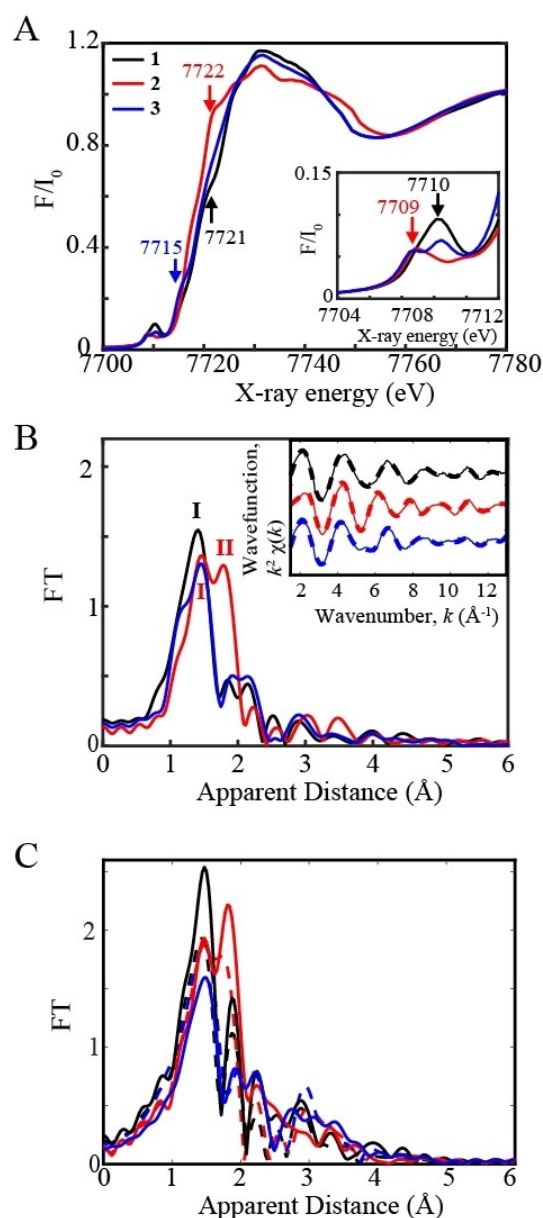


Figure 1. A) Experimental normalized Co K-edge XANES of catalyst **1** (black), **2** (red) and **3** in solid-state. Inset: Zoom-in of the pre-edge regions. B) Fourier transforms of k^2 -weighted Co EXAFS of **1** (black), **2** (red) and **3** (blue). Inset: Back Fourier transformed experimental (solid lines) and fitted (dashed lines) $k^2\chi(k)$ for **1**, **2** and **3** in solid state. Experimental spectra were calculated for k values of 1.5–13 Å^{−1}. C) Simulated FT-EXAFS spectra for **1** (black), **2** (red) and **3** (blue) complexes. Atomic coordinates were obtained from the single crystal XRD structures of the complexes^[15,25] (dashed lines) (Table S2) and from DFT calculations (solid lines) (Table S3, Appendix, Supporting Information)

7710 eV compared to **2** at 7709 eV due to its varied methylene axial ligands and non-centrosymmetric geometry. Indeed non-centrosymmetric complexes have been shown to have an increased intensity in their pre-edge features due to an increase in the metal $4p$ mixing into the $3d$ orbitals contributing towards the electric dipole $1s$ to $4p$ character of this transition.^[23a] By contrast, the Co^{II} catalyst **3** with a d^7 electronic configuration with filled t_{2g} levels and an unpaired electron in the e_g level

displays a multiplet pre-edge as previously observed^[14a] at 7709 and 7710 eV.

The EXAFS spectra of the 3 catalyst precursors are shown in Figure 1B. A prominent peak I with a weak shoulder separated from the Co–C contributions is observed in the EXAFS spectrum of **1** corresponding to the averaged contribution of the Co–N/Co–C and elongated Co–Cl bond distances respectively (black trace). By contrast, two predominant peaks representing the Co–N and Co–Cl contributions can be seen in the catalyst **2**'s EXAFS spectrum. The higher amplitude of peak II in catalyst **2** vs **1** is due to the presence of its 2 distinct Co–Cl distances (Figure 1B, red trace). Catalyst **3** in comparison to **1** and **2** shows only 1 prominent peak within the 1st coordination shell corresponding to the averaged contributions of the Co–N distances (Figure 1B, blue trace).

The EXAFS fits for the extraction of actual bond distances of all 3 complexes are shown in Figure 1B inset, Figure S1 and Table S1. Analysis of the EXAFS spectrum of catalyst **1** resolves 4 Co–N distances at 1.91 Å and 1 lengthened Co–Cl distances at 2.37 Å (Table S1, fit 2, Figure S1A) whereas that of catalyst **2** illustrates improvement of the fit quality with 4 Co–N distances at 1.93 Å and 2 Co–Cl distances at 2.25 Å (Table S1, fits 4 vs 5, Figure S1B). Similarly, EXAFS analysis of catalyst **3** shows 5 Co–N distances at 1.93 Å (Table S1, fit 6, Figure S1C). It is important to remark that the XRD analysis^[15,25] of the 3 Co-based catalysts displays presence of one shortened Co–N distance at ≈ 1.83 – 1.85 Å and 3 more elongated Co–N distances between 1.93 – 2.04 Å (Table S2). Although the EXAFS data resolution is ≈ 0.13 Å and does not enable differentiation between the individual Co–N bond distances, a small shoulder at lower apparent distance could in this case clearly be observed in the EXAFS spectrum of catalyst **3** corresponding to the presence of the shortened Co–N bond distance (Figure 1B).

Importantly, the differences and trends observed in the experimental EXAFS agree well with the EXAFS simulations carried out from XRD analysis and DFT optimized coordinates (Figure 1C, Tables S2, S3, Appendix, Supporting Information).

These findings show that theoretical methods including geometry optimization used for the ground-state structures are consistent with a low spin Co electronic configuration as previously demonstrated from EPR studies^[14e] for this family of tetraazamacrocyclic complexes. DFT employed methods further reproduce the experimental data well showing that they can be reliably used for analysis of the intermediate species of the cobalt complexes' catalytic cycles.

Comparative electronic and structural analysis of the Co-based catalysts in solid vs solution

To gain more insights into the coordination behaviour and ground state structures of these complexes in solution, steady state XANES and EXAFS measurements were performed upon their dissolutions in pure water for 24 h. The chlorido ligands in catalysts **1** and **2** are replaced by aqua ligands as previously^[14a,15] observed which result in the disappearance of the low energy $1s \rightarrow 4p$ shoulder with shakedown

contribution,^[20] and a shift of the rising edge towards higher energy of the XANES spectrum (Figure 2A,B). Catalyst **1** exhibits a 0.35 eV shift in the rising edge from 7719.25 eV to 7719.60 eV at normalized 0.5 fluorescence upon dissolution in H₂O (Figure 2A) whereas **2** displays a larger energy shift of 1.92 eV from 7717.68 to 7719.60 eV (Figure 2B). The greater energy shift manifested in **2** vs **1** is due to the substitution of both of its chlorido ligands by aqua molecules (Figure 2A,B, Top). The shift in the energy position of the XANES absorption edges of **1** and **2** in water is also attributed to their geometrical changes into a more centrosymmetric octahedral complex with two bonded aqua molecules (Figure 2A,B). The enhanced centrosymmetric geometries of **1** and **2** in water are evidenced by the decrease in their pre-edge intensities (Figure 2A,B inset) which arises due to the decrease in the metal 4p mixing into the 3d orbitals.^[23a]

Importantly, **1** and **2** display very similar XANES spectral features after dissolution in H₂O for ≈ 24 h, as illustrated in Figure S2A. This shows that the methylene ligand between the Co and the N atom at the amine position dissociates over time with **1** and **2** turning into a diaqua complex **4** with a hydroxomethylene group at the amine position in H₂O (Figure 2, Top).

TD-DFT XANES simulations were further carried out and the theoretical difference spectral features between an octahedral geometry with 2 bound aqua molecules (compound **4**) and their corresponding structural conformations in solid state (Scheme 1) agree well with experimental data for both catalyst precursors **1** and **2** (Figure S3).

By contrast, **3** shows a dipole-allowed transition in the rising edge at 7715 eV corresponding to the $1s$ to $4p_z$ transition which remains almost the same upon dissolution in water (Figure 3C). This suggests that **3** maintains a square pyramidal geometry with the acetonitrile molecule substituted by an aqua molecule resulting into compound **5** (Figure 2, Top). An additional solvent coordination to the Co complex into an octahedral geometry would have resulted into a degeneracy among the 4p orbitals with the $1s$ to $4p_z$ transition becoming indistinguishable from the $1s$ to $4p_{x,y}$ /white line transition. The pre-edge intensity of **3** in solid vs solution state is furthermore slightly more intense confirming the same pentacoordinated geometry in H₂O (Figure 3C inset). A square planar centrosymmetric geometry in **5** would have resulted in a decreased pre-edge intensity^[23a,24] with a more intense $1s$ to $4p_z$ transition as previously demonstrated.^[22a] The formation of a square pyramidal geometry in complex **5** was further corroborated through TD-DFT XANES difference simulations between a square planar, square pyramidal and octahedral derivative and its corresponding structure in solid state (Figure S4). The best agreement was obtained for a square pyramidal derivative with a bound water molecule as illustrated in Figure S3 and S4, confirming the suitability of the theoretical method to account for the main structural trends in the studied systems.

The EXAFS spectra of **4** generated from catalyst precursors **1** and **2** together with compound **5** formed from precursor **3** are illustrated in Figure 2D–F and overlapped with the corresponding solid-state spectra (Green vs black/red/blue spectra). Catalyst **4** formed from **1** and **2** displays one prominent peak

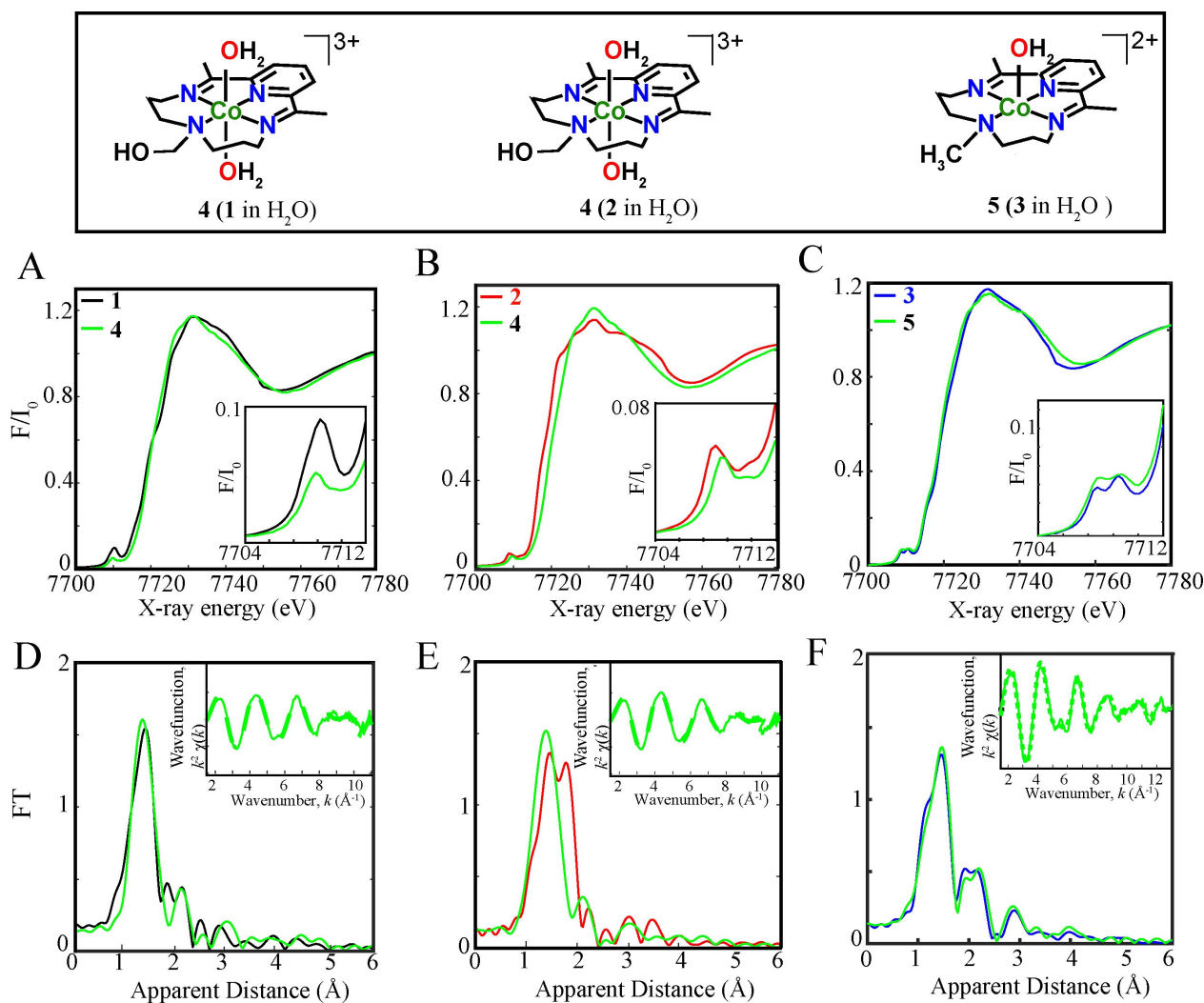


Figure 2. Top. Structures of the Co-based catalysts 1, 2 and 3 upon dissolution in H₂O. Bottom. A–C) Experimental normalized Co K-edge XANES of 1 (A, black) 2 (B, red) and 3 (C, blue) in solid state and upon their respective dissolutions in water over 24 h to form 4 and 5 (B,C, green). Inset: Zoom-in of the pre-edge regions. D–F) Fourier transforms of k^2 -weighted Co EXAFS of 1 (D, black), 2 (E, red) and 3 (F, blue) in solid and upon dissolution in solution to form 4 (D or E, green or red), and 5 (F, green). Inset: Back Fourier transformed experimental (solid lines) and fitted (dashed lines) $k^2 \chi(k)$ for 4 (derived from 1 and 2) together with 5 in H₂O. Experimental spectra were calculated for k values of 1.5–11 Å^{−1} for 4 (formed from 1 and 2) in H₂O, and for k values of 1.5–13 Å^{−1} for 5 in H₂O.

upon water dissolution corresponding to the contribution of both Co–N and Co–O bonds (Figure 2D,E). The EXAFS spectra of 4 generated from 1 and 2 are further similar confirming their comparable structural conformations upon 24 h dissolution in water (Figure S2B). EXAFS analysis of 4 resolves 6 Co–N/O distances at 1.91–1.93 Å and showed improvement of the fit quality upon the addition of 6 Co–N/O vs 5 Co–N and 1 Co–Cl bond distances (Table S1, fits 7/8 vs 9/10, Figure S5A,B). This analysis confirms that both chlorido ligands are fully substituted by aqua ligands upon dissolution in H₂O (Figure 2,Top). By contrast, EXAFS fitting of 5 shows 4 Co–N at 1.95 Å and 1 elongated Co–O distances at 2.22 Å, corresponding to the substituted aqua molecule (Table S1, fit 12, Figure S5C). The fitted Co–N/O distances are in agreement with relaxed structures from DFT geometry optimizations (Table S3, Appendix, Supporting Information) confirming the conformation of a Co octahedral complex with 2 bound water molecules in 4 and

that of a square pyramidal geometry in 5. The differences in the octahedral vs square bipyramidal coordination geometries of the Co^{III} complexes 1 and 2 vs the Co^{II} complex 3 in H₂O are moreover explained by their distinctive electronic configurations.

Conversion of 1 to 4 in H₂O for catalytic H₂ production and time-resolved X-ray absorption spectroscopy of binary mixtures with Ru/Co

Following the steady-state measurements, tr-XAS is applied to directly monitor the electronic and structural conformations of the photo-generated Co^{II} in a binary mixture of Co^{III}-based catalysts precursors 1 and 2 (1 mM) with Ru (5 mM). The binary mixtures are optically pumped at 400 nm in the metal to ligand charge transfer (MLCT) range and probed with X-ray pulses at

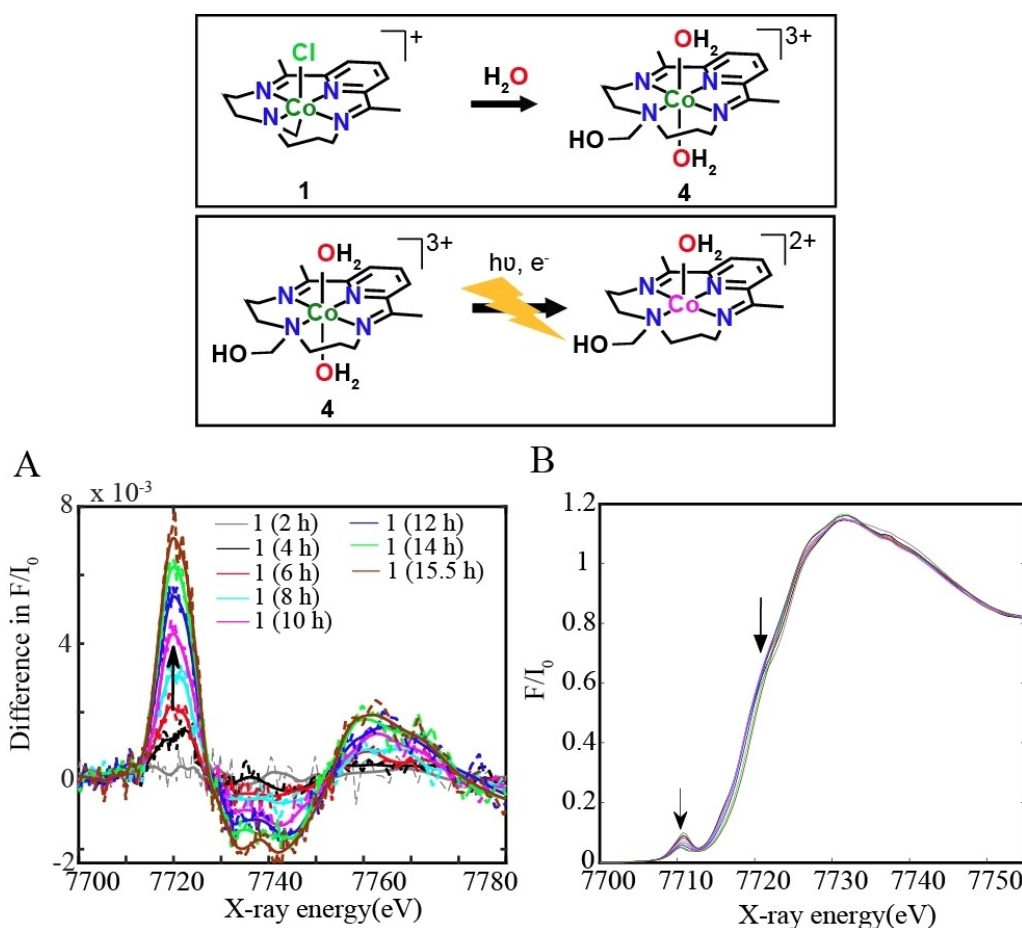


Figure 3. Top. Structural conversion of the Co-based catalyst 1 into 4 upon dissolution in H₂O followed by structure of the Co^{II} intermediate formed upon laser excitation of a binary mixture of 4 with Ru. Bottom. A) Experimental difference spectrum (laser on-laser off) corresponding to the growing Co^{II} transient signal of catalyst precursor 1 (1 mM) with Ru (5 mM) at a delay of 4.59 μs as 1 is dissolved in water for varying times from 2–15.5 h in H₂O. B) Experimental normalized Co K-edge XANES of 1 in H₂O from 2–15.5 h.

several delays from 100 ps to ≈25 μs (Figure S6). XAS spectra of the binary mixtures are collected before and after the laser excitation. By subtracting the laser-off from the laser-on spectrum, a transient signal is obtained for each pump-probe delay and provides information about the photo-induced dynamics, electronic and structural state of the catalyst's excited states (Figure 3A).

Upon light excitation, MLCT from 4 d orbital of Ru to the π* orbital of the ligand followed by intersystem crossing (ISC) to a triplet excited state initially occurs.^[26] This process is followed by electron transfer from the excited photosensitizer to the Co^{III} complex, forming a Co^{II} species. Figure 3A shows the Co tr-XANES spectrum of a binary mixture of catalyst precursor 1 with Ru at an averaged time delay of 4.59 μs between laser and X-ray pulses when 1 is dissolved in water at varying times from 2–15.5 h in H₂O that is leading to its conversion to the diaqua complex 4. A prominent peak at ≈7722 eV together with a broad dip at ≈7740 eV is obtained which corresponds to the formation of the reduced Co^{II} species^[14a,18g] and the ground state bleaching of the Co^{III}, respectively (Figure 3A, Figure S6A). These energy transitions in turn show that the K-edge of the Co center shifts to lower energy, indicating the reduction of Co^{III}

and confirming the formation of Co^{II} through electron transfer from Ru.

Importantly, these measurements demonstrate that the conversion of 1 into the diaqua complex 4 is critical for it to be photoreduced to Co^{II} and be catalytically active for hydrogen production, while compound 1 with two negatively charged ligands (chlorido and methylene bridge) would be unable to accept an electron due to its lower reduction potential. Over time from 2 to 15.5 h, the laser off spectra of catalyst precursor 1 and 2 in H₂O further adopt the same octahedral diaqua structural conformation 4 as previously elaborated and illustrated in Figure 3B and S2. This is remarked by 1's gradual decrease in its pre-edge intensity, loss of its 1s→4p shoulder with shakedown contribution and concomitant shift of its rising edge XANES.

Electronic and Structural Conformations of Co^{II} intermediates derived from Catalyst precursors 1 and 2

A similar transient signal with a maximum time-dependent energy at 7720 eV is obtained for binary mixtures of 4

generated from catalyst precursors **1** and **2** with Ru in water (Figure 4A, Figure S6B). Interestingly, clear changes are not only observed in the oxidation state of the Co catalytic metal site but also in its electronic configuration and coordination environment as indicated by the pre-edge region of the XANES spectrum at lower photon energies of around 7710 eV (Figure 4B). As previously elaborated, Co^{II} with a d⁷ orbital configuration exhibits two pre-edge features observed at 7709 and 7711 eV (Figure 4B). The electronic and geometric information of the photo-generated Co^{II} were first resolved through combined DFT optimizations and TD-DFT XANES simulations. Several possible geometries of the Co^{II} intermediate were explored namely a square planar Co^{II} complex without any

coordinated solvent molecules, a square pyramidal structure with 1 bound water molecule and an octahedral complex with 2 water molecules (Figure S7, Table S3, Appendix, Supporting Information). Importantly, DFT optimization of an octahedral Co^{II} structure illustrates a loosely bound water molecule at 2.35 Å and a second water molecule at a longer distance at 3.37 Å showing that the Co^{II} complex likely maintains a square planar or square pyramidal geometry upon photoexcitation (Table S3, Appendix, Supporting Information). The calculated square planar and square pyramidal Co^{II} XANES derivatives additionally display 2 pre-edge features in the low energy region separated by ≈ 1.5 –2 eV in agreement with the exper-

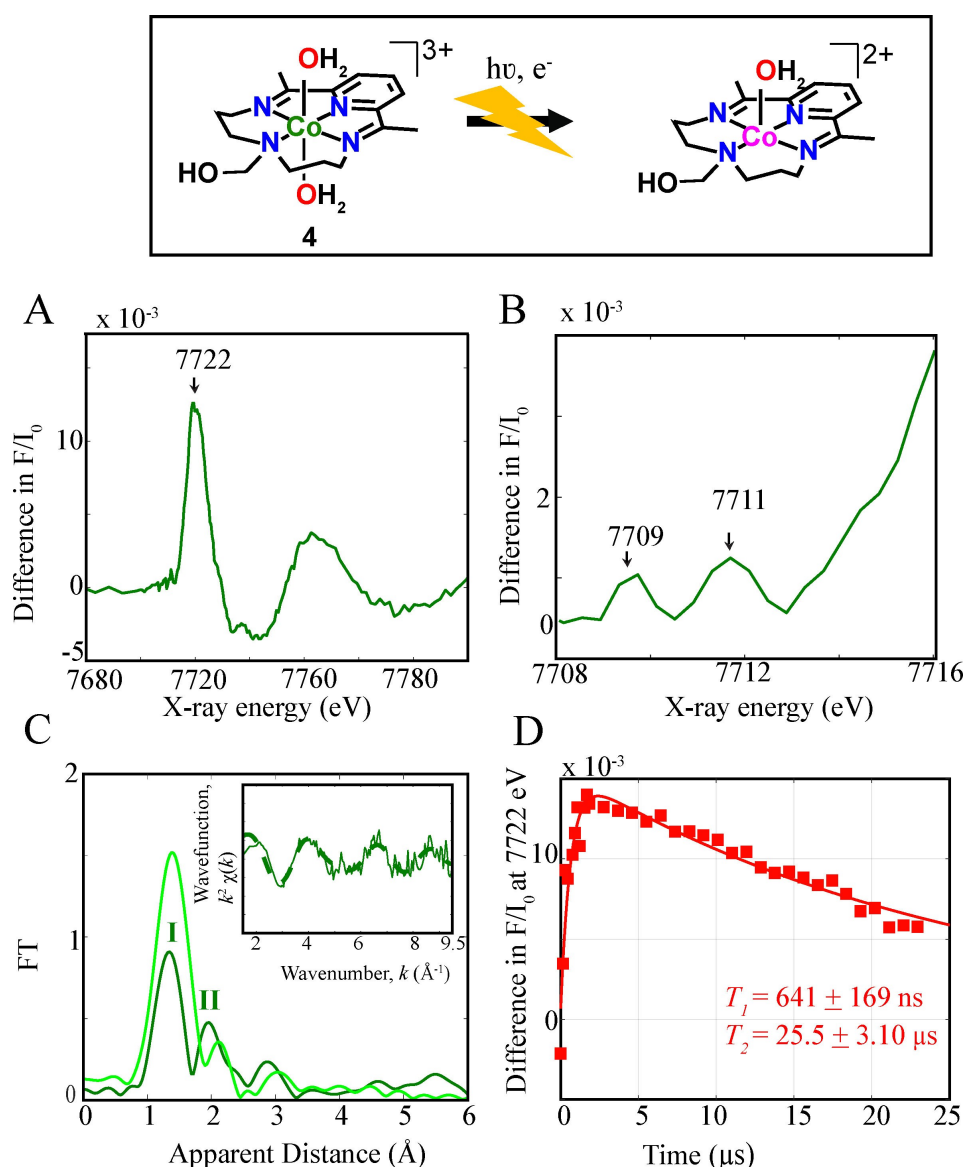


Figure 4. Top. Structure of the Co^{II} intermediate formed upon laser excitation of a binary mixture of the Co^{III} catalysts **4** (1 mM) derived from catalyst precursors **1** and **2**, with Ru(5 mM). Bottom. A) Experimental difference spectrum (laser on-laser off) corresponding to the Co^{II} transient signal for **4** generated from **2** in H₂O at a delay of 4.59 μ s between laser and X-ray pulses. B) Zoom in of the pre-edge region in dark green. C) Fourier transforms of k²-weighted Co EXAFS of the laser off (light green) and reconstructed excited state (dark green) for **4** assuming a percentage excited state fraction of 4.7%. Inset: Back Fourier transformed experimental (solid lines) and fitted (dashed lines) k² $\chi(k)$ for the reconstructed excited state. Experimental spectra were calculated for *k* values of 1.5–9.5 Å^{−1}. D) Pump-probe time delay scans recorded at 7722 eV of a binary mixture [Co^{III}OH₂]⁺/Ru corresponding to the formation and decay of the Co^{II} photoinduced species for **4** generated from **2** in H₂O. Kinetic fits *T*₁ and *T*₂ of the Co^{II} formation and decay processes are shown.

imental data, while the octahedral derivative shows a broader pre-edge peak.

To ascertain the structure of the photogenerated Co^{II} , time-resolved EXAFS analysis was further carried out. The excited state fractions of the Co^{II} intermediates were determined by comparing the relative intensity of the transient signal with that of a reference chemically reduced Co^{II} complex (Figure S8, Figure S10A). The peak intensity of the normalized transient signal between a pure Co^{II} complex and the laser-on spectra of **4** derived from catalyst precursors **1** and **2** in H_2O is 0.28 such that a proportion of the excited state of around 4.4% and 4.7% were respectively estimated in their laser on spectra and further used to plot the actual or reconstructed spectra (Figure S9, Figure S10B). Similar percentages of the Co^{II} reduced species were determined upon integrating the pre-edge region of the excited state and comparing to the pure Co^{II} chemically generated complex (Figure S8). These two analysis procedures thus confirm the correct percentage of excited state fractions used in the estimation of the laser on spectra.

The derived transient states of **4** moreover both show two prominent peaks I and II corresponding to the Co–N and elongated Co–O distances (Figure 4C, Figure S10B). Analysis of the EXAFS peaks within the first coordination sphere of the reconstructed EXAFS spectrum of **4** derived from precursor **1** shows 4 Co–N bond distances at 1.93 Å and 1 elongated Co–O bond distance at 2.20 Å (Figure S10B, Table S1, Fit 14, Figure S11A). Similarly, EXAFS analysis of the Co^{II} derivative of **4** formed from **2** shows 4 Co–N distances at 1.93 Å and an elongated Co–O distance at 2.21 Å (Figure 4C, Table S1, Fit 16, Figure S11B). These distances are in agreement with DFT optimized coordinates of a square pyramidal Co^{II} intermediate with a hydroxomethylene amine group (Table S3). Its calculated EXAFS profile additionally agrees well with the experimental spectrum (Figure S12) and rules out the formation of a Co^{II} square planar structure.

The kinetics for the formation and decay of the Co^{II} species were further investigated in binary mixtures composed of **4** from precursors **1** and **2** with Ru by fixing the photon energy to 7722 eV, corresponding to the formation of Co^{II} , and varying the time delays between the laser and X-ray pulses (Figure 2D, Figure S10C). The formation and decay kinetics for the Co^{II} species are around the same within error bars in both binary mixtures and appear promptly within 903 ± 215 ns (precursor **1**) and 641 ± 169 ns (precursor **2**) and decay within 29.4 ± 5.10 μs (precursor **1**) and 25.5 ± 3.10 μs (precursor **2**) (Figure S10C, Figure 4D). This kinetics analysis determines the lifetimes of the Co^{II} intermediates which are long-lived enough to form the Co^{I} active species that enter the catalytic cycle (Scheme 2).

Tr-XAS studies of a previously reported^[14a] Co tetraazamacrocyclic catalyst with a hydrogen directly connected to the amino group of the macrocyclic ligand were also conducted under the same experimental conditions as catalyst **4** in a binary mixture composed of 1 mM of the Co catalyst and 5 mM Ru. Kinetic studies for the formation of the photogenerated Co^{II} reveal similar formation and decay lifetimes of 605 ± 105 ns and 23.8 ± 2.72 μs (Figure S13) as **4** showing that the recombination

lifetimes of Co^{II} with Ru^{III} are not dependent on the hydrogen or hydroxomethylene amine substituent being used.

Photo-induced optical transient absorption spectroscopy in a complete photocatalytic system

Prior to tr-XAS, OTA spectroscopy was performed to investigate the photo-induced electron transfer dynamics of **4** under photocatalytic conditions with ascorbic acid/sodium ascorbate mixtures ($\text{H}_2\text{Asc}/\text{NaHAsc}$, 1:1) (Figure S14–S16). These conditions mimic conditions where molecular hydrogen can be evolved and have previously shown excellent results in combination with this family of Co-based catalysts.^[14a,15] Upon addition of ascorbate, the Co^{III} catalyst **4** is instantly reduced to its Co^{II} derivative due to its sufficiently strong reduction potential. Importantly, **1** and **2** as in previous experiments were both dissolved in H_2O for ≈ 24 h to ensure its full conversion to **4**. The necessity for **1** to be dissolved *a priori* in H_2O in order to be active for H_2 production was further illustrated in a complete photocatalytic system with the ascorbate electron donor (Figure S17). Catalytic activity tests of a ternary mixture composed of 0.05 mM **1**, 0.5 mM Ru and 0.55 mM (1:1 $\text{H}_2\text{Asc}/\text{NaHAsc}$) showed an induction time during which **1** gradually starts to convert into the diaqua complex **4** (Figure S18).

Following laser excitation of the complete photocatalytic system, we observe a broad negative band centered at 625 nm which corresponds to the fluorescence of the excited photosensitizer state, Ru^* (Figure S14A–C). The excited state is formed before the first time point in the nanosecond OTA experiment, and decays within 333 ± 3 nanoseconds (Figure S15B), consistent with literature values.^[27] The lifetime of the excited photosensitizer decreases by a factor of only 1.4 to 245 ± 2 ns and 247 ± 2 ns in the presence of the Co catalyst **4** from precursors **1** and **2** respectively (Figure S15C,D). The excited Ru-based photosensitizer Ru^* subsequently reacts with ascorbate to form the reduced state of Ru, $[\text{Ru}(\text{bpy})_2(\text{bpy}^-)]^+$, which is observed as an absorption band at ≈ 500 nm in the OTA spectrum (Figure S14A–C). The reduced Ru^- displays formation and decay times of 175 ± 8 ns and 50.6 ± 0.1 μs (Figure S16A,B) in the absence of the Co-based catalysts (Figure S16B). Importantly, the Ru^- decay becomes significantly faster to 2.80 ± 0.02 μs (Figure S16C) and 2.78 ± 0.02 μs (Figure S16D) in the presence of **4** formed from **1** and **2** respectively. The 18-fold decreased decay time (Figure S16) supports the electron transfer from Ru^- to Co^{II} and illustrates the reductive quenching mechanism to be the predominant quenching pathway within the family of Co-based catalysts as previously observed.^[14e] The similar OTA formation and decay lifetimes obtained for catalyst precursors **1** and **2** further corroborate their comparable structural conformations into **4** in H_2O as previously discussed (Figure S15C,D, Figure S16C,D).

Importantly, although OTA experiments discriminated between oxidative and reductive Ru^* quenching mechanisms, simultaneously monitoring the formation of the Co^{I} intermediate was not possible due to its overlapping absorbing bands with Ru and its relatively low extinction coefficient, thus

emphasizing the power of tr-XAS in resolving the electronic signatures of the generated catalytic intermediates.

Electronic and Structural Characterization of Co^I Intermediate derived from Catalyst Precursors 1, 2 and 3

Tr-XAS was thus applied to study the 3 catalytic complexes under similar photocatalytic conditions. Interestingly, tr-XAS of the catalytic mixtures containing the Co^{II} catalysts (1 mM), Ru photosensitizer (5 mM) and the sacrificial electron donor H₂Asc/NaHAsc (1.1, 75 mM) in H₂O (Figure 5) shows the formation of a reduced species at lower energy range which correspond to the formation of the Co^I derivative. On the one hand, a similar transient signal with a peak energy at 7716 eV is obtained for the photocatalytic mixtures of **4** generated from precursors **1** and **2** (Figure 5A, black and red traces, respectively). On the other hand, the transient signal of the ternary photocatalytic mixture of **5** features two prominent peaks at 7714 and 7719 eV (Figure 5A, blue trace) showing that the Co^I derivative of catalyst **5** adopts a different structural conformation than **4**.

The kinetics for the formation of the Co^I species were similarly further investigated in all 3 photocatalytic mixtures by

fixing the photon energies to the peak energies of the Co^I transient signals and varying the laser and X-ray pulse delays. The decay of the Co^I species could be fitted with 2 time constants in 1:1 ratio assuming both charge recombination processes with the ascorbate radical and protonation as previously illustrated.^[14c] The charge recombination lifetimes of **4** and **5** are similar, ranging between ≈ 1.4 – $1.9 \mu\text{s}$ due to the same concentrations of Co catalysts (1 mM) and H₂Asc/NaHAsc (75 mM) being employed. Furthermore the formation and decay kinetics of the Co^I species in the ternary mixtures of **4** from precursors **1** and **2** are expectedly the same appearing within $485 \pm 69.0 \text{ ns}$ (**1**) and $528 \pm 114 \text{ ns}$ (**2**) and decaying within $9.86 \pm 0.96 \mu\text{s}$ (**1**), and $8.35 \pm 1.65 \mu\text{s}$ (**2**) (Figure 5B,C). The time scales of formation of Co^I in the tr-XAS experiments are much shorter than that obtained from OTA experiments due to the higher concentrations of the Co catalysts and Ru employed in the X-ray experiments for a sufficient transient signal response together with the diffusion-governed nature of these interactions (Figure 5, Figures S14–S16). Importantly, the formation of the Co^I species in the photocatalytic mixture of **5** appears within similar time range of $462 \pm 100 \text{ ns}$ but decays at a much slower rate at $35.0 \pm 8.74 \mu\text{s}$ (Figure 5D).

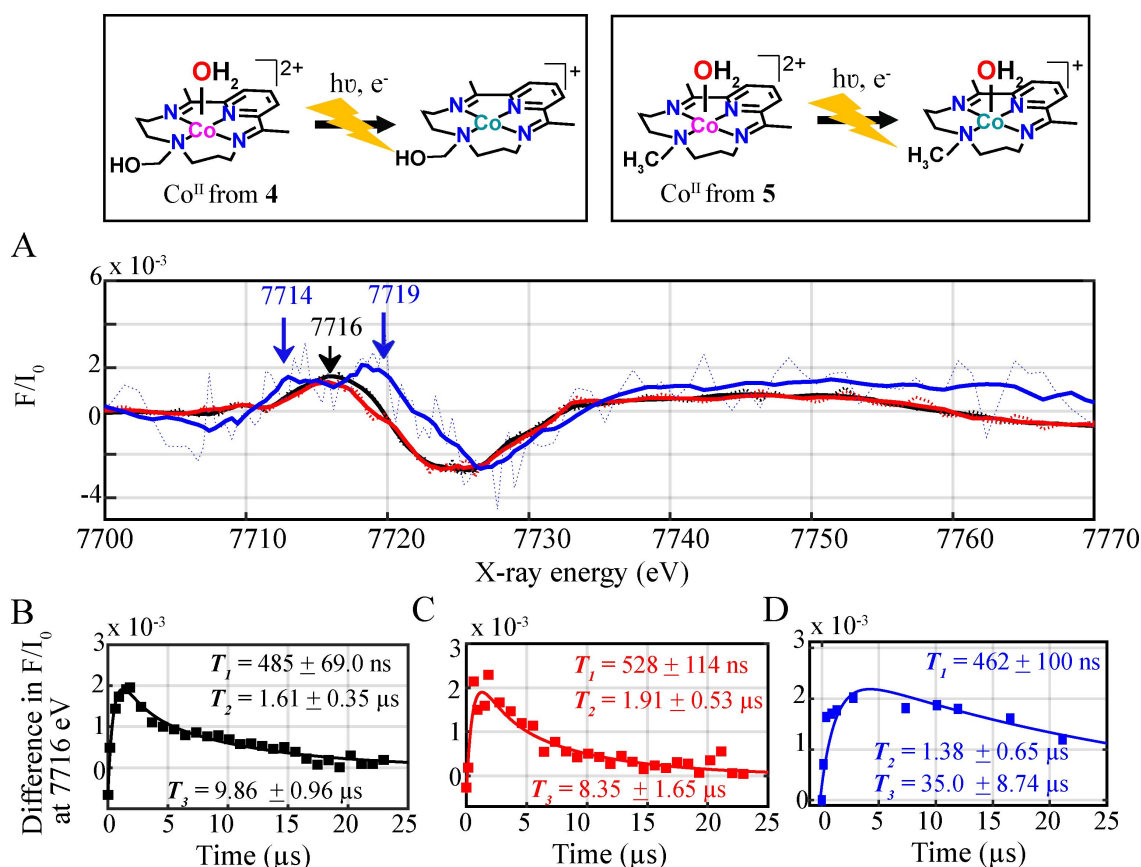


Figure 5. Top. Structure of the Co^I derivative formed upon laser excitation of a complete photocatalytic mixture of Left. **4** (generated from **1** and **2**), Right. **5** (generated from **3**). Bottom. A) Experimental transient signal of Co^I intermediate generated upon illumination of a complete photocatalytic mixture composed of **4** (formed from **1** (black) and **2** (red)) together with **5** (blue). X-ray kinetics taken at 7716 eV of a ternary mixture Co (1 mM) Ru (5 mM) /H₂Asc/NaHAsc (75 mM) corresponding to the formation and decay of the Co^I photoinduced species of a photocatalytic mixture composed of **4** formed from **1** (B), **2** (C,D). **5** at a delay of 11.5 μs between laser and X-ray pulses. Kinetic fits T_1 , T_2 , T_3 of the Co^I formation, charge recombination with the ascorbate radical and protonation lifetimes are shown. The decay lifetimes T_2 and T_3 for **4** and **5** could be fitted in a 1:1 ratio.

According to the different hydrogen evolution pathways,^[14a] a Co^{III} hydride can be formed after protonation of the Co^I intermediate and generate hydrogen via heterolytic or homolytic pathways by reacting with a proton or a second Co^{III} hydride molecule, respectively (Scheme 2). Alternatively, it can be reduced to form a Co^{II} hydride species that can analogously react through homolytic or heterolytic mechanism. It is however important to remark that while the one-electron reduction of a Co^{III} hydride molecule to form a Co^{II} hydride species can occur under continuous light irradiation, this process is not possible within our experimental conditions as a single laser pulse is hereby employed to excite the ternary photocatalytic mixture. The formation of the Co^{II} hydride species can however occur through the bimolecular reaction of the photogenerated Co^I and Co^{III} hydride species as illustrated in Scheme 2.

The formation of the Co^{III} hydride species has previously been determined for this family of tetraazamacrocyclic complexes under both electrochemically^[15] and photochemically^[14a] induced hydrogen evolution catalysis. The 4-fold slower decay of the Co^I species in the photocatalytic system with catalyst 5 vs 4 (Figure 5C–D) hereby indicates its slower protonation to form the elusive hydride species that leads to the hydrogen evolution reaction. As shown from the Co^I experimental transient signals at various times (Figure S18A–C), the spectral features for the elusive hydride species were not observed under our experimental conditions due to its high reactivity. Given the 78 ps pulse duration (full width at half maximum) of the X-rays, we speculate that the lifetime of the hydride species can be shorter than 78 picoseconds as previously determined.^[14a]

Altogether, these results suggest that the hydroxomethylene group in catalyst 4, generated from 1 and 2, helps in the formation of the H–H bond in comparison to 5 (derived from 3) that possesses the methyl group. In order to further confirm the active role of the pendant proton relay in facilitating the Co^I protonation rate and catalytic rate, tr-XAS studies of the Co tetraazamacrocyclic catalyst with a hydrogen directly connected to the amino group of the macrocyclic ligand^[14a] were additionally conducted under the same experimental conditions as catalysts 4 and 5. Tr-XAS of a complete photocatalytic system composed of the Co complex (1 mM), Ru (5 mM), H₂Asc/NaHAsc (1:1, 75 mM) showed the formation of a Co^I reduced species at 7713.9 eV as previously^[14a] observed (Figure S19) and a similar charge recombination lifetime of $1.20 \pm 0.377 \mu\text{s}$ as catalysts 4 and 5. Importantly, the kinetics for the decay of the Co^I species for the Co complex with -NH group directly linked to the macrocyclic ligand is $2.47 \pm 0.765 \mu\text{s}$ and faster by a factor of ≈ 4 and 14 in comparison to catalysts 4 and 5 with the hydroxomethylene and methyl amine substituents, respectively (Figure S19). Thus, the catalytic rate of hydrogen evolution catalysts could be enhanced through the introduction of substituents containing proton relays at the amine position that aid towards H–H bond formation.

These results further show that the rate limiting step of these processes is the formation of the intermediate Co^{III} hydride that is so reactive that it rapidly combines with a proton or another hydride molecule. Unlike previous studies,^[14a]

the starting Co^{III} complex was not observed due to the presence of a larger and excess amount (75 mM) of sodium ascorbate/ascorbic acid which helps in reducing the Co catalyst (1 mM) more efficiently.

The excited state fractions of the Co^I intermediates between the laser pump excitation and X-ray probing were too low (less than 1%) to reconstruct their EXAFS and structural conformations (Figure 5A, and Figure 6A,B). The tr-XANES spectra were thus combined with TD-DFT XANES simulations to extract the electronic and geometric information about the photo-generated Co^I. Several possible geometries of the Co^I intermediate were theoretically explored as illustrated in Figures 6 and S20.

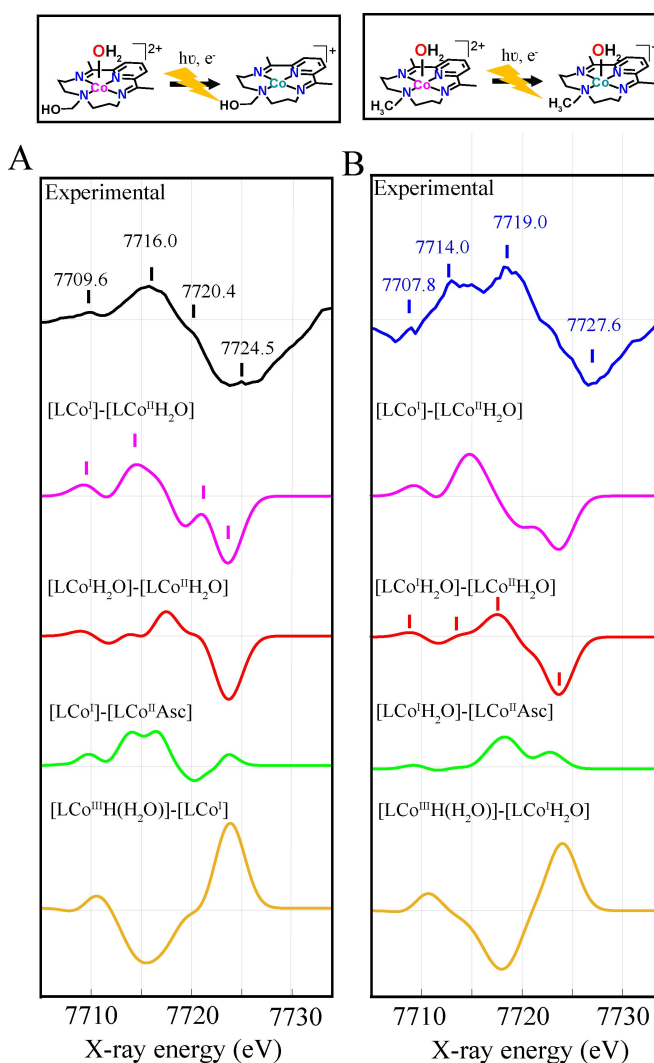


Figure 6. Top. Structure of the Co^I derivative formed upon laser excitation of a complete photocatalytic mixture of Left. 4 (generated from 1 and 2 with conc of 1 mM) with Ru (5 mM)/H₂Asc/NaHAsc (75 mM). Right. 5 (generated from 3) with [Ru(bpy)₃]²⁺/H₂Asc/NaHAsc. Comparison of the experimental difference spectrum taken at an averaged delay of 11.5 μs of 4 (A, black) 5 (B, in blue) after laser excitation, and TD-DFT simulated difference spectra corresponding to the formations of a square planar [LCo^I] (in pink) and square pyramidal [LCo^I(OH₂)] (in red) geometries from a square pyramidal [LCo^{II}(OH₂)] for 4 and a square planar [LCo^I] intermediate for 5 together with a square planar [LCo^I] intermediate formed from a square pyramidal [LCo^{II}(Asc)] derivative (in green) and an octahedral [LCo^{III}H(H₂O)] hydride derivative formed from a square planar [LCo^I] complex (in dark yellow).

The formation of a Co^{I} square planar or square pyramidal complex generated from a Co^{II} square pyramidal complex with a bound water or ascorbate molecule for catalysts **4** and **5** were importantly considered (Figure 6A,B, Figure S20). As shown in Figure 6A, there is poor agreement between the experimental spectrum and theoretical simulation for a Co^{I} square pyramidal structure generated from a Co^{II} square pyramidal complex bound to one water (red trace) or ascorbate (green trace) molecule for catalyst **4**.

However, the simulation for a Co^{I} square planar structure without any coordinated solvent molecules (pink trace in Figure 6A) resolves the intensities in the pre-edge and rising edge features well confirming the formation of such a geometry in **4**. By contrast, the best agreement for the Co^{I} derivative in **5** was that of a square pyramidal complex with a loosely coordinated water molecule at 2.36 Å generated from an analogous Co^{II} geometry.

The formation of a Co^{I} square planar or square pyramidal geometry is consistent with single crystal X-ray structures of similar intermediates for CO_2 reduction reactions^[28] and tr-XAS results of similar tetraazamacrocyclic^[14a] and polypyridyl^[17b] Co-based catalysts for proton reduction.

Additional spectral comparisons of a Co^{III} hydride species generated from a Co^{I} square planar and square pyramidal derivatives were further carried out (yellow traces in Figure S6A,B, Figure S20). As illustrated in Figure 6 and S20, the hydride spectral features were not observed, confirming its lifetime to be less than the 78 ps pulse duration of the X-rays. It is worth mentioning that although the EXAFS of the Co^{I} derivatives could not be resolved, the pre-edge and rising edge features coupled with our TD-DFT XANES calculations and DFT optimizations provide an excellent fingerprint of the local coordination of the Co^{I} excited states.

Conclusions

The electronic and structural conformations of a series of Co-based catalysts with tetraazamacrocyclic ligands are reported in the solid state and in solution through steady-state X-ray absorption near edge structure (XANES) and extended X-ray absorption fine structure analysis (EXAFS). The experimental results are further supported by theoretical XANES and time-dependent DFT (TD-DFT) calculations. Upon dissolution in water, the chlorido ligands in catalysts **1** and **2** with the methylene and hydroxomethylene groups are substituted by aqua ligands to form compound **4** with an octahedral geometry with two water molecules at a distance of $\approx 1.91\text{--}1.93$ Å. Critically, the Co^{III} catalyst **1** with the methylene group has to be dissolved in H_2O for a period of several hours for it to be catalytically active for hydrogen production. In contrast, the acetonitrile molecule in catalyst **3** with the methyl amine substituent is replaced by an aqua molecule to form compound **5** with a square pyramidal geometry. Upon photoexcitation with Ru, **4** generated from both **1** and **2** is reduced to a Co^{II} species and undergo a Co–O bond elongation of ≈ 0.3 Å.

We additionally monitored the rise time kinetics of the Co^{II} intermediates in **4**, formed from both precursors **1** and **2**, to be 641–913 ns followed by its decay to be within 25.5–29.4 μs . The study of the complete multimolecular system in the presence of sodium ascorbate/ascorbic acid electron donor (Ru/Co/Asc) showed the formation of a Co^{I} derivative with a square planar geometry in **4** and exposed a square pyramidal structure with a loosely coordinated water molecule at 2.36 Å in **5**. While the formation of the Co^{I} intermediate lied within the same time span 462–528 ns for all 3 multimolecular catalytic systems, the decay of the Co^{I} derivative was 4-fold slower and around 35.0 μs vs 8.35–9.86 μs for catalyst **5** and **4**, respectively. The faster decay of the Co^{I} species in the multimolecular assemblies with catalyst **4** vs **5** (Figure 6) illustrates its faster protonation to form the elusive hydride species.

These results show that both protonation and catalytic rate efficiency can be enhanced through the introduction of terminal hydrogen containing substituents at the amine position that function as efficient proton relays for the formation or cleavage of the H–H bond.^[29] The rate limiting step in all 3 multimolecular systems were further found to involve the protonation of the Co^{I} intermediate. These findings are crucial towards increasing our understanding of charge separation dynamics in Ru–Co photocatalytic systems and is an important step in the rationalization and design of future cost-effective Co-based molecular catalysts that are fully functional in pure water.

Experimental Section

Steady-state and time-resolved XAS on the solution complexes

Steady-state and time-resolved XAS spectra were collected at the beamline 11 ID-D^[16] of the Advanced Photon Source using the output from an APS standard undulator (3.3 cm period length and a total length of 2.4 m). The samples were circulated through a stainless-steel nozzle into a free-flowing 650 μm cylindrical jet inside an airtight aluminium chamber, and continuously degassed with nitrogen. This sample handling technique ensures proper sample recovery such that the subsequent laser pulse can hit a “fresh” sample position. Cooled running water from a chiller was additionally circulated around the jacketed sample flask to prevent heating damage of the complexes by radiation. Several batches of ≈ 20 mL of all 3 catalysts were dissolved in water over 24 h and were measured in H_2O alone, in binary mixture with Ru and in ternary mixtures with Ru $\text{H}_2\text{Asc}/\text{NaHAsc}$. No X-ray radiation and laser-induced damage was observed over the course of several hours of XANES and EXAFS data collection.

The X-ray fluorescence signals were collected with two APDs positioned at 90° on both sides of the liquid jet, and a combination of Z-1 filters and soler slits with conical geometry were used to reduce the background from elastically scattered X-rays. The radiation was in this case monochromatized by a Si(111) crystal monochromator. The upstream beam intensity (I_0) was measured with a gas ionization detector filled with pure nitrogen. The Co XAS energy was once again calibrated by the first maximum of the derivative of the Co metal XANES spectrum at 7708.20 eV.

The time-resolved experiments were all carried out using the 24 bunch mode of APS (in top up mode with a constant 102 mA ring current) which consists of a train of X-rays separated at 6.5 MHz. On the one hand, the binary and ternary mixtures composed of catalysts **4** generated from both **1** and **2** were pumped at 400 nm wavelength using a regenerative amplified laser with 10 kHz repetition rate 1.6 ps-full-width half maximum (FWHM) pulse length and laser power of 630 mW. On the other hand, the ternary mixture composed of catalyst **5** was pumped with a 3 KHz repetition rate laser with similar pulse length and with laser power of 430 mW. The instrument response function (IRF) is determined by the laser and X-ray FWHM: $\sqrt{(\text{Laser Pulse width})^2 + (\text{X-ray Pulse width})^2}$. The pulse duration of the laser is very short (1.6 ps) compared to that of the X-ray pulse (≈ 78.8 ps) such that the IRF is equivalent to ≈ 78.8 ps.

This timing mode was suitable for this type of experiments in which the 153 ns time separation between two adjacent ≈ 78.8 ps X-ray pulses are long enough for the avalanche Photodiode (APD) detectors to resolved individual X-ray pulses. The X-ray and laser beam was spatially overlapped with an X-ray spot size of $100\text{ }\mu\text{m(V)} \times 450\text{ }\mu\text{m(H)}$ and a maximum laser focus to the central plane of the cylindrical jet of $170\text{ }\mu\text{m(V)} \times 550\text{ }\mu\text{m(H)}$. With a liquid flow speed of around 3.5 m/s, the pumped laser volume was calculated to move out of the FWHM region in around 25 μs .

This temporal range ensured that the excited state volume was probed more at the centre and less at the edges where the excitation fraction would be less, due to movement of the sample. Beamline 11 ID-D has an automated data digitization system which allows for all X-ray pulses after laser excitation to be collected. The detailed description of the experimental set up and data acquisition has been previously reported.^[30] Such a system, together with the larger X-ray beam spot size, was very useful for our experiments, as multiple X-ray pulses after laser excitation were averaged to monitor the dynamics for the formation and decay of the Co^{II} and Co^{I} excited states in the nano-microsecond time regime. The delay between the laser and X-ray pulses was adjusted by a programmable analogy delay line (PDL-100A-20NS, Colby Instruments) and a digital delay line (Highland V851 digital delay/pulse generator).

Acknowledgements

D.M acknowledges funding from the Ramon y Cajal grant RYC2020-029863-I through the Instituto de Ciencia de Materiales de Madrid, Consejo Superior de Investigaciones Científicas (CSIC-ICMM), PIE grant from CSIC-ICMM (20226AT001), and the Spanish Ministerio de Ciencia, Innovación y Universidades grants (PID2019-111086RA-I00, TED2021-132757B-I00, PID2022-143013OB-I00). X.Z. and C.L. acknowledge funding from DOE, Office of Science, Basic Energy Sciences, Chemical Sciences, Geosciences, and Biosciences Division under contract no. DE-AC02-06CH11357. A. P acknowledges grant ref. PID2021-126560NB-I00 (MCIU/AEI/FEDER, UE), and grants refs. 2017-T1/IND-5432 and 2021-5A/IND-20959 (Comunidad de Madrid through TALENTO program). S.D. acknowledges the Max Planck Society for funding. C.G.S acknowledges funding from the Ramon y Cajal grant RYC2019-027423-I. A.L acknowledges financial support from Ministerio de Ciencia e Innovación through projects PID2019-111617RB-I00 (MCIN/AEI/10.13039/501100011033) and SO-CEX2019-000925-S (MCIN/AEI/10.13039/5011000110). This research used resources of beamline 20 BM-B and 11 ID-D of the Advanced Photon Source (APS); a U.S.

Department of Energy (DOE) Office of Science User Facility operated for the DOE Office of Science by Argonne National Laboratory under Contract No. DE-AC02-06CH11357. We also thank Dr. Rebeca Gomez Castillo and Dr. Benjamin Van Kuiken for help with sample changes at the 11 ID-D beamline of the APS. The DFT calculations were performed in the Scientific Computing Center (CCC) Universidad Autónoma Madrid, (Cat-DesignProject, PI: D. Moonshiram, A.Picón)

Conflict of Interests

The authors declare no conflict of interest.

Data Availability Statement

The data that support the findings of this study are available in the supplementary material of this article.

Keywords: Co hydrogen evolution catalysts • Time-resolved X-ray absorption spectroscopy • TD-DFT calculations • Optical transient absorption spectroscopy

- [1] A. Thapper, S. Styring, G. Saracco, W. Rutherford, B. Robert, A. Magnuson, W. Lubitz, A. Lobet, P. Kurz, A. Holzwarth, S. Fiechter, H. d Grott, S. Campagna, A. Braun, H. Bercegol, V. Artero, *Green* **2010**, *3*, 43–57.
- [2] G. Nicoletti, N. Arcuri, G. Nicoletti, R. Bruno, *Energy Convers. Manage.* **2015**, *89*, 205–213.
- [3] W. T. Eckenhoff, W. R. McNamara, P. Du, R. Eisenberg, *Biochim. Biophys. Acta Bioenerg.* **2013**, *1827*, 958–973.
- [4] G. W. Crabtree, M. S. Dresselhaus, *MRS Bull.* **2008**, *33*, 421–428.
- [5] a) P. Du, J. Schneider, P. Jarosz, R. Eisenberg, *J. Am. Chem. Soc.* **2006**, *128*, 7726–7727; b) D. Dolui, S. Khandelwal, P. Majumder, A. Dutta, *Chem. Commun.* **2020**, *56*, 8166–8181; c) F. Lakadamyali, E. Reisner, *Chem. Commun.* **2011**, *47*, 1695–1697; d) T. Lazarides, T. McCormick, P. Du, G. Luo, B. Lindley, R. Eisenberg, *J. Am. Chem. Soc.* **2009**, *131*, 9192–9194; e) W. M. Singh, M. Mirmohades, R. T. Jane, T. A. White, L. Hammarström, A. Thapper, R. Lomoth, S. Ott, *Chem. Commun.* **2013**, *49*, 8638–8640.
- [6] a) Z. Han, F. Qiu, R. Eisenberg, P. L. Holland, T. D. Krauss, *Science* **2012**, *338*, 1321–1324; b) M. A. Gross, A. Reynal, J. R. Durrant, E. Reisner, *J. Am. Chem. Soc.* **2014**, *136*, 356–366; c) M. A. Gross, C. E. Creissen, K. L. Orchard, E. Reisner, *Chem. Sci.* **2016**, *7*, 5537–5546.
- [7] a) C. Wan, B. M. Leonard, *Chem. Mater.* **2015**, *27*, 4281–4288; b) H. I. Karunadasa, E. Montalvo, Y. Sun, M. Majda, J. R. Long, C. J. Chang, *Science* **2012**, *335*, 698–702; c) H. I. Karunadasa, C. J. Chang, J. R. Long, *Nature* **2010**, *464*, 1329–1333; d) J. Kibsgaard, T. F. Jaramillo, *Angew. Chem. Int. Ed.* **2014**, *53*, 14433–14437.
- [8] M. L. Singleton, J. H. Reibenspies, M. Y. Darensbourg, *J. Am. Chem. Soc.* **2010**, *132*, 8870–8871.
- [9] K. L. Mulfort, A. Mukherjee, O. Kokhan, P. Du, D. M. Tiede, *Chem. Soc. Rev.* **2013**, *42*, 2215–2227.
- [10] V. Artero, M. Chavarot-Kerlidou, M. Fontecave, *Angew. Chem. Int. Ed.* **2011**, *50*, 7238–7266.
- [11] C. C. L. McCrory, C. Uyeda, J. C. Peters, *J. Am. Chem. Soc.* **2012**, *134*, 3164–3170.
- [12] Y. Sun, J. P. Bigi, N. A. Piro, M. L. Tang, J. R. Long, C. J. Chang, *J. Am. Chem. Soc.* **2011**, *133*, 9212–9215.
- [13] C.-F. Leung, Y.-Z. Chen, H.-Q. Yu, S.-M. Yiu, C.-C. Ko, T.-C. Lau, *Int. J. Hydrogen Energy* **2011**, *36*, 11640–11645.
- [14] a) D. Moonshiram, C. Gimbert-Suriñach, A. Guda, A. Picon, C. S. Lehmann, X. Zhang, G. Doumy, A. M. March, J. Benet-Buchholz, A. Soldatov, A. Lobet, S. H. Southworth, *J. Am. Chem. Soc.* **2016**, *138*, 10586–10596; b) M. Sandroni, R. Guert, K. D. Wegner, P. Reiss, J.

- Fortage, D. Aldakov, M. N. Collomb, *Energy Environ. Sci.* **2018**, *11*, 1752–1761; c) R. Gueret, C. E. Castillo, M. Rebarz, F. Thomas, A.-A. Hargrove, J. Pécaut, M. Sliwa, J. Fortage, M.-N. Collomb, *J. Photochem. Photobiol. B* **2015**, *152*, 82–94; d) C. Gimbert-Suriñach, J. Albero, T. Stoll, J. Fortage, M.-N. Collomb, A. Deronzier, E. Palomares, A. Llobet, *J. Am. Chem. Soc.* **2014**, *136*, 7655–7661; e) S. Varma, C. E. Castillo, T. Stoll, J. Fortage, A. G. Blackman, F. Molton, A. Deronzier, M.-N. Collomb, *Phys. Chem. Chem. Phys.* **2013**, *15*, 17544–17552.
- [15] S. Grau, M. Schilling, D. Moonshiram, J. Benet-Buchholz, S. Luber, A. Llobet, C. Gimbert-Suriñach, *ChemSusChem* **2020**, *13*, 2745–2752.
- [16] L. X. Chen, X. Zhang, *J. Phys. Chem. Lett.* **2013**, *4*, 4000–4013.
- [17] a) D. Moonshiram, A. Guda, L. Kohler, A. Picon, S. Guda, C. S. Lehmann, X. Zhang, S. H. Southworth, K. L. Mulfort, *J. Phys. Chem. C* **2016**, *120*, 20049–20057; b) Z.-J. Li, F. Zhan, H. Xiao, X. Zhang, Q.-Y. Kong, X.-B. Fan, W.-Q. Liu, M.-Y. Huang, C. Huang, Y.-J. Gao, X.-B. Li, Q.-Y. Meng, K. Feng, B. Chen, C.-H. Tung, H.-F. Zhao, Y. Tao, L.-Z. Wu, *J. Phys. Chem. Lett.* **2016**, *7*, 5253–5258.
- [18] a) D. Moonshiram, A. Picón, A. Vazquez-Mayagoitia, X. Zhang, M.-F. Tu, P. Garrido-Barros, J.-P. Mahy, F. Avenier, A. Aukauloo, *Chem. Commun.* **2017**, *53*, 2725–2728; b) D. Moonshiram, P. Garrido-Barros, C. Gimbert-Suriñach, A. Picón, C. Liu, X. Zhang, M. Karnahl, A. Llobet, *Chem. Eur. J.* **2018**, *24*, 6464–6472; c) P. Gotico, D. Moonshiram, C. Liu, X. Zhang, R. Guillot, A. Quaranta, Z. Halime, W. Leibl, A. Aukauloo, *Chem. Eur. J.* **2020**, *26*, 2859–2868; d) M. Rentschler, S. Iglesias, M.-A. Schmid, C. Liu, S. Tschierlei, W. Frey, X. Zhang, M. Karnahl, D. Moonshiram, *Chem. Eur. J.* **2020**, *26*, 9527–9536; e) S. Iglesias, A. Gamonal, A. Abudulimu, A. Picón, E. Carrasco, D. Écija, C. Liu, L. Luer, X. Zhang, J. S. Costa, D. Moonshiram, *Chem. Eur. J.* **2020**, *26*, 10801–10810; f) L. Velasco, L. Llanos, P. Levín, A. Vega, J. Yu, X. Zhang, L. Lemus, D. Aravena, D. Moonshiram, *Phys. Chem. Chem. Phys.* **2021**, *23*, 3656–3667; g) J. Zhao, S. De Kreijger, L. Troian-Gautier, J. Yu, W. Hu, X. Zhang, B. Elias, D. Moonshiram, *Chem. Commun.* **2022**, *58*, 8057–8060.
- [19] a) R. A. Bair, W. A. Goddard, *Phys. Rev. B* **1980**, *22*, 2767–2776; b) L.-S. Kau, D. J. Spira-Solomon, J. E. Penner-Hahn, K. O. Hodgson, E. I. Solomon, *J. Am. Chem. Soc.* **1987**, *109*, 6433–6442.
- [20] a) F. Juliá, *ChemCatChem* **2022**, *14*, e202200916; b) M. Uchikoshi, K. Shinoda, *Struct.* **2019**, *30*, 945–954.
- [21] S. DeBeer George, L. Basumallick, R. K. Szilagy, D. W. Randall, M. G. Hill, A. M. Nersissian, J. S. Valentine, B. Hedman, K. O. Hodgson, E. I. Solomon, *J. Am. Chem. Soc.* **2003**, *125*, 11314–11328.
- [22] a) W. Hu, D. Wang, Q. Ma, B. J. Reinhart, X. Zhang, J. Huang, *J. Photochem. Photobiol. A* **2022**, *11*, 100132; b) P. Chandrasekaran, K. P. Chiang, D. Nordlund, U. Bergmann, P. L. Holland, S. DeBeer, *Inorg. Chem.* **2013**, *52*, 6286–6298.
- [23] a) T. E. Westre, P. Kennepohl, J. G. DeWitt, B. Hedman, K. O. Hodgson, E. I. Solomon, *J. Am. Chem. Soc.* **1997**, *119*, 6297–6314; b) K. E. Loeb, T. E. Westre, T. J. Kappock, N. Mitic, E. Glasfeld, J. P. Caradonna, B. Hedman, K. O. Hodgson, E. I. Solomon, *J. Am. Chem. Soc.* **1997**, *119*, 1901–1915.
- [24] S. DeBeer George, P. Brant, E. I. Solomon, *J. Am. Chem. Soc.* **2005**, *127*, 667–674.
- [25] C.-K. Poon, S. S. T. Liao, *J. Chem. Soc. Dalton Trans.* **1978**, 1180–1185.
- [26] N. H. Damrauer, G. Cerullo, A. Yeh, T. R. Boussie, C. V. Shank, J. K. McCusker, *Science* **1997**, *275*, 54–57.
- [27] A. Mukherjee, O. Kokhan, J. Huang, J. Niklas, L. X. Chen, D. M. Tiede, K. L. Mulfort, *Phys. Chem. Chem. Phys.* **2013**, *15*, 21070–21076.
- [28] a) D. C. Lacy, C. C. L. McCrory, J. C. Peters, *Inorg. Chem.* **2014**, *53*, 4980–4988; b) M. Zhang, M. El-Roz, H. Frei, J. L. Mendoza-Cortes, M. Head-Gordon, D. C. Lacy, J. C. Peters, *J. Phys. Chem. C* **2015**, *119*, 4645–4654.
- [29] M. L. Helm, M. P. Stewart, R. M. Bullock, M. R. DuBois, D. L. DuBois, *Science* **2011**, *333*, 863–866.
- [30] E. D. Kinigstein, G. Jennings, C. A. Kurtz, A. M. March, X. Zuo, L. X. Chen, K. Attenkofer, X. Zhang, *Rev. Sci. Instrum.* **2021**, *92*, 085109.

 Manuscript received: May 18, 2023

Revised manuscript received: July 28, 2023

Accepted manuscript online: August 7, 2023

Version of record online: August 24, 2023